Available online at BCREC website: https://bcrec.id

Bulletin of Chemical Reaction Engineering & Catalysis, 18 (4) 2023, 582-592

Research Article

Lanthanum-substituted Cobalt Ferrite Established by the Co-precipitation Process: Annealing Temperature Adjustment of Structural, Magnetic, and Dye Removal Characteristics

Ramadona Rahmawati[1], Adiana Musadewi[1], Nurdiyantoro Putra Prasetya[1], S. Suharno[2], Sri Budiawanti[2], Dwi Teguh Rahardjo[2], R. Riyatun[1], U. Utari[1], Yofentina Iriani[1], N. Nuryani[1], Budi Purnama[1,*]

[1]Physics Department, Faculty of Mathematics and Natural Sciences, Universitas Sebelas Maret, Jl. Ir. Sutami 36A, Kentingan, Jebres, Surakarta 57126, Indonesia.
[2]Physics Education Department, Faculty of Teacher Training and Education, Universitas Sebelas Maret, Jl. Ir. Sutami 36A Kentingan Surakarta 57126, Indonesia.

Received: 25th July 2023; Revised: 17th October 2023; Accepted: 18th October 2023
Available online: 23rd October 2023; Published regularly: December 2023

Abstract

Co-precipitation process was used for the synthesis of lanthanum-substituted cobalt ferrite nanoparticles at several annealing temperatures (T_a), i.e., 200 °C, 300 °C, and 400 °C, for 5 h. XRD spectral depicted that the produced nanoparticles sample indicates a single phase of fcc inverse spinel conforming to ICDD No 22-1086. The crystallite size (D) calculation at the strongest peaks shows the increase in enhancing the T_a i.e., 18.99 nm, 19.90 nm, and 23.21 nm for 200 °C, 300 °C, and 400 °C, respectively. The FTIR results showed absorption band at the tetrahedral site, υ_1 ~575 cm^{-1} and the octahedral site, υ_2 ~474 cm^{-1}. The absorption bands indicate that the lanthanum ions have successfully replaced the Fe^{3+} cations in the original cobalt ferrite structure. According to the hysteresis loop, the coercive field's (H_C) magnitude falls from 700 Oe down to 550 Oe as T_a increases. This result is consistent with the anisotropy constant which decreased from 0.77×10^4 erg/cm^3 to 0.56×10^4 erg/cm^3. The obtained nanoparticles also showed superior performance (much larger than 95%) for dye removal of Congo red.

Keywords: Cobalt Ferrite; Co-precipitation; Nanoparticles; Dye Removal

How to Cite: R. Rahmawati, A. Musadewi, N.P. Prasetya, S. Suharno, S. Budiawanti, D.T. Rahardjo, R. Riyatun, U. Utari, Y. Iriani, N. Nuryani, B. Purnama (2023). Lanthanum-substituted Cobalt Ferrite Established by the Co-precipitation Process: Annealing Temperature Adjustment of Structural, Magnetic, and Dye Removal Characteristics. *Bulletin of Chemical Reaction Engineering & Catalysis*, 18(4), 582-592 (doi: 10.9767/bcrec.19638)

Permalink/DOI: https://doi.org/10.9767/bcrec.19638

1. Introduction

Magnetic ferrite are generally classified into four subgroups; spinel ferrite, hexagonal ferrite, garnet, and orthoferrite [1]. Individual material exhibits its own unique structural, magnetic, and electrical properties. Spinel ferrite is one material that is currently widely studied in research. The fundamental formula for spinel ferrite is MFe_2O_4; M is the divalent cation, which includes Co, Mg, Mn, Ni, and Zn [2]. Spinel ferrite is also a member of the Fd-3m space group face-centered cubic (fcc) crystal [3]. Two interstitial sites can be discovered in spinel ferrite: the tetrahedral site (A-site) and the octahedral site (B-site) [4]. The distribution of anions between

* Corresponding Author.
Email: bpurnama@mipa.uns.ac.id (B. Purnama)

sites A and B dependence on annealing temperature (T_a), synthesis procedure as well as substation other metal cation [5,6]. The number of available states at A-site (Fe^{3+}) in cobalt ferrite is 64, yet only 8 cations are occupied. While B-site (Fe^{3+} + Co^{2+}) has 32 states, it only has 16 cations [7]. So, either the cations redistribution due to physical treatment or the other metal cations substitution will modify their magnetic properties [3].

Theoretically, the magnetic moment associated with saturation magnetization is 3 nB overall, with 5 nB and 8 nB at both of the A and B sites, respectively [8]. In the case of other metal cation substitutions, the suitability of the ionic radius and size of the interstices determines the mechanism of magnetic characteristics modification. Metal cations owing zero magnetic moments, such as Lanthanum, are an intriguing research material that can be substituted in cobalt ferrite [9].

The Co^{2+} and Fe^{3+} ions occupy the octahedral site of cobalt ferrite. La^{3+} tends to replace ions at octahedral sites. When La^{3+} enters an octahedral site, it tends to displace the Fe^{3+} ion, because it has the same ion size. In the case of inverted spinel at the tetrahedral site, ion charging is more dominant over the 3+ ion so that Fe^{3+} moves to the tetrahedral site after La^{3+} replaces the Fe^{3+} ion at the octahedral site [10]. Cobalt ferrite has interesting characteristics that open up application opportunities [7], such as; permanent magnets [11], magnetic sensors [12], photocatalyst [13], antibacterial [14], drug delivery [15], and MRI agent contrast [16].

Cobalt ferrite nanoparticles can be synthesized using a variety of techniques. Most popular methods are co-precipitation [17–19], sol-gel [20–22], and hydrothermal [23–25]. As part of this study, the synthesis of cobalt ferrite material with lanthanum substitution carried out using the co-precipitation method due to well-controlled distribution of dopants and crystallite size [26]. Additionally, the coprecipitation method was chosen because it can produce large *Hc* and smaller *Ms* as the particle size increases depending on the NaOH concentration [27].

In this study, the synthesis of lanthanum substituted cobalt ferrite nanoparticles using variations in the T_a will be reported. The concentration taken is the most optimal which can maximally modify the structure and magnetic properties. Increasing the concentration above 10% will give rise to a secondary phase on sample [28].

2. Materials and Methods

2.1 Experimental

Lanthanum substituted cobalt ferrite ($CoLa_{0.1}Fe_{1.9}O_4$) nanoparticles were produced utilizing the co-precipitation method. $Fe(NO_3)_3.9H_2O$ (Merck), $Co(NO_3)_2.6H_2O$ (Merck), and $La(NO_3)_3.6H_2O$ (Merck) were the components utilized in the synthesis; they were dissolved in double-distilled water and stirred for 10 min. In order to generate a precipitate, the NaOH solution (4.8 M) was added dropwise while being continuously after being heated to 95 °C and stirred (250 rpm) [27]. This precipitate was collected, cleaned with ethanol to get rid of the salts that had been dissolved, and then overnight dried at 100°C. The sample was then annealed for 5 h at temperatures of 200 °C, 300 °C, and 400 °C at a heating rate of 10 °C/s. The powder was then hand-milled in a marble mortar for 2 h to obtain the final product before being physically characterized.

2.2 Material Characterizations

The crystalline structure of the $CoLa_{0.1}Fe_{1.9}O_4$ nanoparticles is evaluated using an X'Pert PRO PANalytical X-ray diffractometer (using Cu-Kα radiation with a wavelength of = 1.54). The XRD patterns were acquired in the 2θ = 20–70° range, with a step size of 0.02° and a duration of 0.7 s per step. A Shimadzu IR Prestige 21 FTIR spectroscope in the 350–4,000 cm^{-1} range was used to characterize the oxide bonds in the sample. The hysteresis loop of the M-H curve measurements was taken at room temperature using an Oxford VSM1.2 H vibrating-sample magnetometer.

2.3 Dye Removal Study

The Congo red dye removal properties were evaluated by using Ultraviolet Visible Spectroscopy (UV Vis). The dye removal performance was evaluated using a 20 ppm Congo red solution as a test dye model by considering both absorption and irradiated-ultraviolet-light-photocatalyst processes.

2.4 Equations for Calculations

The crystallite size can be calculated by Scherrer's formula:

$$D = \frac{0.9\lambda}{\beta \cos\theta} \quad (1)$$

where, D is the crystallite size, the magnitude of wavelength (λ Cu-Kα is 0.154060 nm, β is the full width at half maximum (FWHM), and

θ is the Bragg angle of diffraction. Furthermore, the lattice parameters are obtained from the following equation.

$$a = d_{hkl}\sqrt{h^2 + k^2 + l^2} \quad (2)$$

where, a is the lattice parameters, d is the interplanar distance, and *(h, k, l)* is the Miller indices of the nanoparticles. Other parameters that can be obtained from XRD analysis are density (ρ_x) and lattice strain (ε) which calculate the following equation [29].

$$\rho_x = \frac{8M}{2a^3} \quad (3)$$

$$\varepsilon = \frac{\beta}{4\tan\theta} \quad (4)$$

where, M is the molecular weight of the nanoparticles and a^3 is the cell volume of the $CoLa_{0.1}Fe_{1.9}O_4$ nanoparticle using various the T_a treatments. Meanwhile, the specific surface area (S) can be obtained from the relationship between D and ρ_x, i.e., $S = 6/(\rho_x \times D)$ [30]. The results of the calculation are summarized in Table 2.

Using the approach described by Waldron, the force constants for the tetrahedral site (k_t) and octahedral site (k_o) were calculated [31]:

$$k_t = 7.62 \times M_1 \times v_1^2 \times 10^{-7}\ N/m \quad (5)$$

$$k_o = 10.62 \times \left(\frac{M_2}{2}\right) \times v_2^2 \times 10^{-7}\ N/m \quad (6)$$

where, M_1 and M_2 are the molecular weights of the cations on the tetrahedral and octahedral sites, respectively. Additionally, the FTIR data can be applied to determine the average force constants magnitude (F) using the following equation [32]:

$$F = \frac{2k_o + k_t}{3} \quad (7)$$

The netto moment magnetic, n_B and magnetic anisotropy, K calculate following the equation [33].

$$n_B = \frac{M \times Ms}{5585} \quad (8)$$

$$K = \frac{Hc \times Ms}{0.98} \quad (9)$$

In multidomain, the relationship between the coercivity field and the anisotropy constant is expressed in the following equation:

$$Hc = e + \frac{f}{D} \quad (10)$$

where, e and f are constants, and D is the size of the crystallite. Therefore, the coercivity decreases as the crystallite size increases, causing the anisotropy constant to also decrease [34].

Furthermore, the results of the percentage reduction (η) in the photocatalyst test are calculated using the following equation [30]:

$$\eta = \frac{(A_o - A_t)}{A_o} \times 100\% \quad (11)$$

where, A_o is the initial absorbance and A_t is the final absorbance. The percentage reduction re-

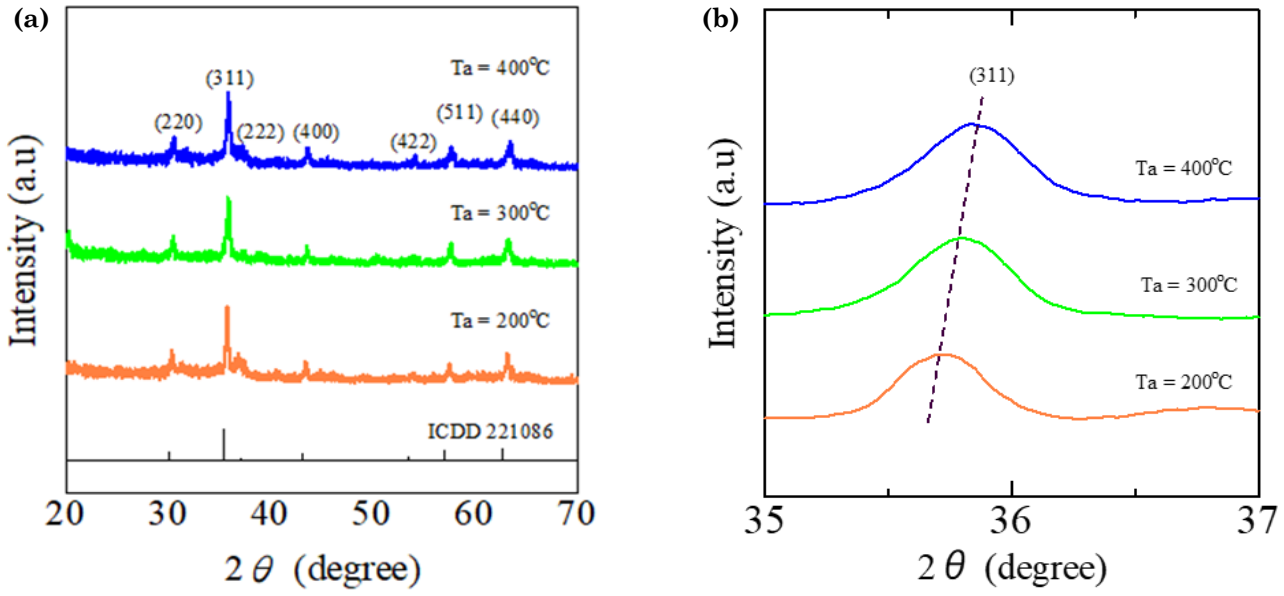

Figure 1. (a) XRD patterns of the $CoLa_{0.1}Fe_{1.9}O_4$ nanoparticles at 200 °C, 300 °C, and 400 °C; (b) The strongest peak shift of the $CoLa_{0.1}Fe_{1.9}O_4$ nanoparticles at 200 °C, 300 °C, and 400 °C.

sults of the $CoLa_{0.1}Fe_{1.9}O_4$ photocatalyst at different T_a are listed in Table 6.

3. Results and Discussion

3.1 XRD Analysis of $CoLa_{0.1}Fe_{1.9}O_4$ Nanoparticles

Figure 1(a) presents XRD patterns of the $CoLa_{0.1}Fe_{1.9}O_4$ nanoparticles using various the T_a treatments (200 °C, 300 °C, and 400 °C). All patterns conform to ICDD 22-1086 which indicates that all samples belong to the face-centered cubic (fcc) crystal structure with the space group Fd-3m [35]. Rietveld refined results using Fullprof™ software have also confirmed that $CoLa_{0.1}Fe_{1.9}O_4$ nanoparticles have a fcc crystal structure with a space group Fd-3m (Figure 2), refinement parameters are provided in Table 1. The results show the magnitude of χ^2 (goodness of fit) $CoLa_{0.1}Fe_{1.9}O_4$ at 200 °C, 300 °C, and 400 °C were 1.67, 1.65, and 1.63, respectively; this result is close to a magnitude of 1 which means it supports the goodness of refinement [6]. The results of the analysis using ICDD and Fullprof™ software justify that La^{3+} ions can successfully replace Fe^{3+} ions in cobalt ferrite nanoparticles.

The strongest peak (311) was used to calculate the crystallite size (Equation (1)) and lattice parameters (Equation (2)) shown in Table 2. Other parameters that can be obtained from XRD analysis are density (Equation (3)) and lattice strain (Equation (40). The molar mass of the material created in all materials is the same according to stoichiometry. However, in Table 2, when the annealing temperature treatment causes changes in structural parameters such as crystallite size and lattice parameters, the impact on other parameters also changes.

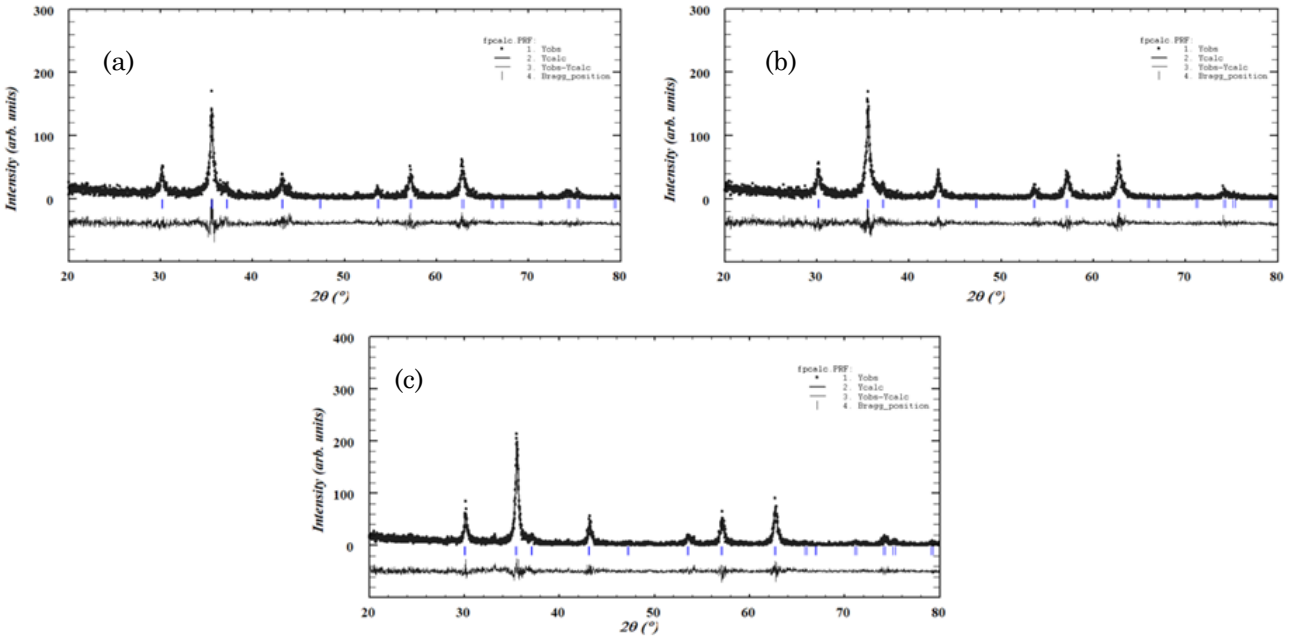

Figure 2. Rietveld refined XRD patterns of the $CoLa_{0.1}Fe_{1.9}O_4$ nanoparticles at (a) 200 °C, (b) 300 °C, and (c) 400 °C.

Table 1. The Rietveld analysis by Fullprof of the $CoLa_{0.1}Fe_{1.9}O_4$ nanoparticles.

T_a (°C)	a=b=c (Å)	R_{wp}	R_{exp}	R_B	χ^2
200	8.359	40.1	28.7	15.8	1.67
300	8.373	36.9	26.5	14.9	1.65
400	8.370	33.0	23.7	12.3	1.63

Table 2. The crystallite size (D), lattice parameters (a), density (ρ_x), lattice strain (ε), and specific surface area (S) of the $CoLa_{0.1}Fe_{1.9}O_4$ nanoparticles.

T_a (°C)	D (nm)	a (Å)	ρ_x (g/cm^3)	ε (10^{-3})	S (m^2/g)
200	18.99	8.338	5.568	5.96	56.74
300	19.90	8.316	5.613	5.67	53.71
400	23.21	8.343	5.559	4.88	46.50

The crystallite sizes of the $CoLa_{0.1}Fe_{1.9}O_4$ nanoparticles using various T_a treatments at 200 °C, 300 °C, and 400 °C was 18.99 nm, 19.90 nm, and 23.21 nm, respectively. With an increase in a certain T_a, the crystallite sizes may increase [((19.90−18.99)/18.99)×100% = 4.79% and ((23.21−19.90)/19.90)×100% = 15.53%], which may be related to an increase in the internal energy of the crystal structure that can lead to atomic diffusion. Atomic diffusion particles may aggregate into larger particles [36]. Other, increasing the T_a speeds up the crystallization process resulting in a larger crystallite size [37,38]. Furthermore, the lattice parameters acquire random magnitudes with an increase in the T_a around ~8.3 Å which is confirmed by the random shift of the strongest peak in Figure 1(b). Similar results were obtained when calculating the density magnitudes. This randomness is allegedly due to the formation of random oxygen vacancies so that the compaction of the material becomes less regular [35]. Meanwhile, the lattice strain decreased with increasing the T_a at 200 °C, 300 °C, and 400 °C were 5.96×10^{-3}, 5.67×10^{-3}, and 4.48×10^{-3}, respectively. The decrease that occurred was 5.11% [$((5.96\times10^{-3} - 5.67\times10^{-3}) / 5.67\times10^{-3})\times100\%$] and 26.56% [$((5.67\times10^{-3} - 4.48\times10^{-3}) / 4.48\times10^{-3})\times100\%$]. This difference is attributed to the change in crystallite size, which cause lattice strain. A decrease in lattice strain and an increase in crystallite size are caused by the material's improved crystallization [39].

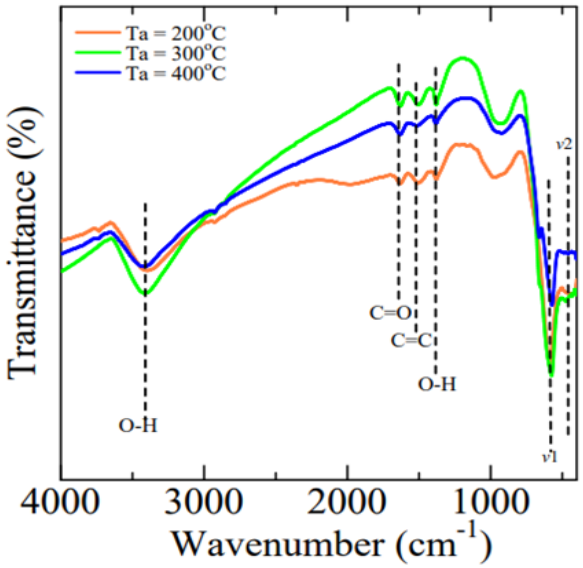

Figure 3. FTIR Spectrum of the $CoLa_{0.1}Fe_{1.9}O_4$ nanoparticles at 200 °C, 300 °C, and 400 °C.

La^{3+} and Fe^{3+} have differences in ionic radius. The rare earth metal La^{3+} is a nonmagnetic cation because it does have 3d electrons, but the ion size is larger than Fe^{3+} and Co^{2+}. So, a small amount of the element La^{3+} in cobalt ferrite can cause lattice strains in the material and cause structural changes that impact its magnetic properties. Substituting larger ions limits the very high nucleation rate of cobalt ferrite due to lattice [40]. Thus, the size of the crystallites is one of the factors that causes changes in the lattice strain. Furthermore, the specific surface area magnitude of the $CoLa_{0.1}Fe_{1.9}O_4$ decreased with increasing the T_a at 200 °C, 300 °C, and 400 °C were 56.74 m^2/g,

Table 3. Absorption bands of FTIR the $CoLa_{0.1}Fe_{1.9}O_4$ nanoparticles.

T_a (°C)	Absorption (cm^{-1})	Mode of vibration
200	3393.9	O−H stretching
	1631.85	C=O stretching
	1505.51	C=C stretching
	1379.16	O−H bending
	589.28	Me−O tetrahedral site
	471.62	Me−O octahedral site
300	3417.04	O−H stretching
	1633.78	C=O stretching
	1506.47	C=C stretching
	1380.13	O−H bending
	575.78	Me−O tetrahedral site
	474.51	Me−O octahedral site
400	3417.04	O−H stretching
	1631.85	C=O stretching
	1515.15	C=C stretching
	1382.06	O−H bending
	571.92	Me−O tetrahedral site
	493.8	Me−O octahedral site

53.71 m²/g, and 46.50 m²/g, respectively. This decrease is due to the expansion of the crystals and the sample's high surface-to-volume ratio [41,42].

3.2 FTIR Analysis of $CoLa_{0.1}Fe_{1.9}O_4$ Nanoparticles

Figure 3 shows the FTIR spectrum of the $CoLa_{0.1}Fe_{1.9}O_4$ nanoparticles with the T_a at 200 °C, 300 °C, and 400 °C. The FTIR analysis obtained absorption band results as shown in Table 3. The absorption bands appeared at the tetrahedral site, υ_1 of 471.62 cm^{-1}, 474.51 cm^{-1}, and 493.80 cm^{-1}; the octahedral site, υ_2 of 589.28 cm^{-1}, 575.78 cm^{-1}, and 571.92 cm^{-1} at the T_a of 200 °C, 300 °C, and 400 °C, respectively. The primary absorption band range supports the cobalt ferrite-based structure [19,43]. It is also claimed that the La^{3+} cation has been successful in switching the Fe^{3+} cations from the cobalt ferrite's initial structure [2].

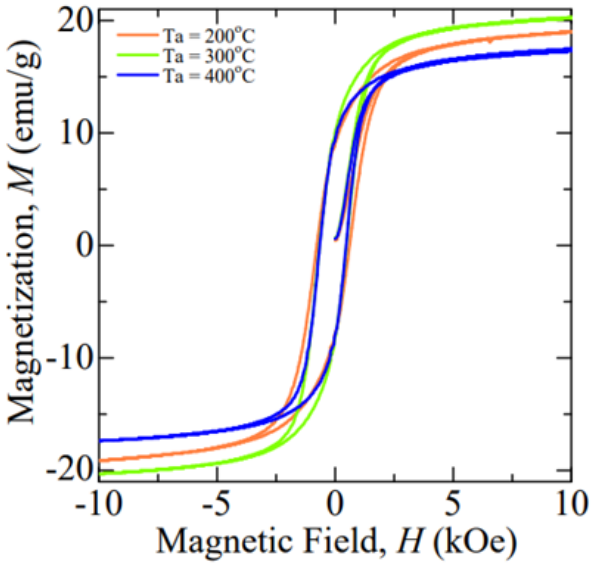

Figure 4. The typical *M-H* curves of co-precipitated the $CoLa_{0.1}Fe_{1.9}O_4$ nanoparticles for different T_a at 200 °C, 300 °C, and 400 °C.

Table 4 shows that the tetrahedral force constant decreased with an increase in the T_a, i.e., 148.58 N/m, 141.85 N/m, and 139.95 N/m; whereas the octahedral force constant increased, i.e. 151.57 N/m, 153.43 N/m, and 166.16 N/m, at the T_a of 200 °C, 300 °C, and 400 °C, respectively. The decrease in the tetrahedral force constant is caused by a decrease in the interatomic distance (Me−O) at the tetrahedral sites, while the increase in the octahedral force constant is affected by an increase in the bond length (Me−O) [44]. The movement of ions to these two sites causes the absorption to change.

3.3 VSM Analysis of $CoLa_{0.1}Fe_{1.9}O_4$ Nanoparticles

Figure 4 presents the hysteresis loop of the $CoLa_{0.1}Fe_{1.9}O_4$ nanoparticles with the T_a at 200 °C, 300 °C, and 400 °C. Table 5 displays the findings from the evaluation of the hysteresis loop, including the coercive field (H_C), saturation magnetization (M_S), remanent magnetization (M_R), magnetic moment (n_B), and magnetic anisotropy constant (K).

The H_C of the $CoLa_{0.1}Fe_{1.9}O_4$ nanoparticles obtains a decrease with increasing the T_a, i.e., 700 Oe, 560 Oe, and 550 Oe at the T_a of 200 °C, 300 °C, and 400 °C, respectively. The calculations of the magnetic anisotropy constant, which decreases with increasing the T_a, provide support for the H_C results. The squareness ratio magnitudes for the $CoLa_{0.1}Fe_{1.9}O_4$ at the T_a were 200 °C, 300 °C, and 400 °C were 0.43,0.44, and 0.49, respectively; the results obtained have a magnitude smaller than 0.5 implies that all nanoparticles are multi-domain [6,45]. The reduction of the H_C can occur due to changes in particle size and domain-wall pinning might cause crystalline imperfections in the multi-domain state [34]. The magnetic properties resulting from La^{3+} substitution which carries 4*f* electron spins on cobalt ferrite are caused by the dominant super exchange in-

Table 4. FTIR parameters of the $CoLa_{0.1}Fe_{1.9}O_4$ nanoparticles.

T_a (°C)	υ_1 (cm^{-1})	υ_2 (cm^{-1})	k_t (N/m)	k_o (N/m)	F (N/m)
200	589.28	471.62	148.58	151.57	150.57
300	575.78	474.51	141.85	153.43	149.57
400	571.92	493.80	139.95	166.16	157.42

Table 5. Magnetic parameters of the $CoLa_{0.1}Fe_{1.9}O_4$ nanoparticles samples.

T_a (°C)	H_C (Oe)	M_S (emu/g)	M_R (emu/g)	M_R/M_S	n_B (μ_B)	K(×10⁴) (erg/cm³)
200	700	19.05	8.37	0.43	0.83	0.77
300	560	20.30	8.99	0.44	0.88	0.67
400	550	17.45	8.70	0.49	0.76	0.56

teraction via oxygen ions between cations in A-site and B-site. This magnetic behavior is largely regulated by 3*d* electron spin coupling. The emergence of 3*d*-4*f* electron spin coupling

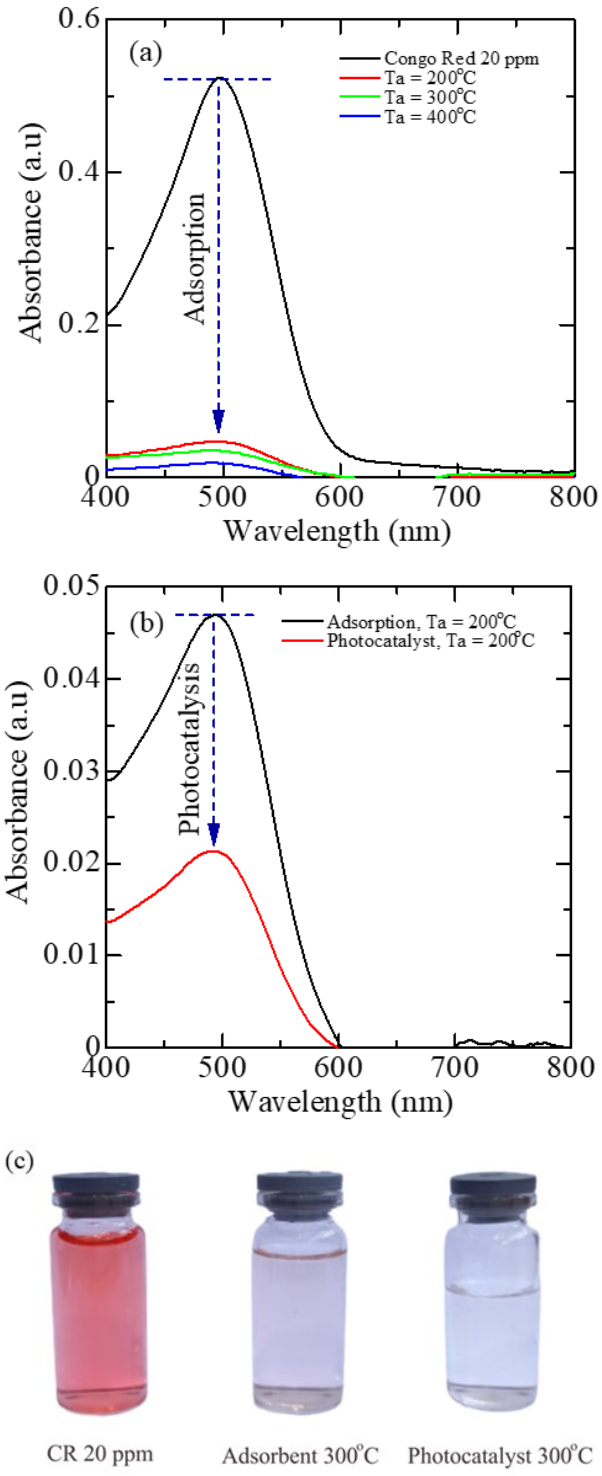

Figure 5. Dye removal characteristic of the $CoLa_{0.1}Fe_{1.9}O_4$ nanoparticles, (a) adsorption properties for different the T_a at 200 °C, 300 °C, and 400°C; (b) typical photocatalytic properties for the T_a of 200 °C; (c) Visual-photograph of the best Congo red dye removal for the T_a of 300 °C.

can be expected through the substitution of small amounts of rare earth cations [40].

Redistribution of cations is related to changes in magnetization. Meanwhile, changes in physical properties can be associated with Hc due to changes in the magneto crystalline anisotropy constant. The anisotropy constant depends on the size of the crystallites. Heat treatment increases the annealing temperature, and it can reduce the anisotropy constant because the crystallite size decreases. This is possible because of the existence of multi magnetic domains in the material.

3.4 Dye Removal Analysis of $CoLa_{0.1}Fe_{1.9}O_4$ Nanoparticles

Figure 5 shows the dye removal characteristic of the $CoLa_{0.1}Fe_{1.9}O_4$ nanoparticles. Figure 5(a) can be seen that there was a decrease in the degradation results of the Congo red pollutant for overnight time. Furthermore, the photocatalyst test was performed by irradiating UV light for 10 min and the results were obtained in the form of a decrease in the degradation magnitude of all the $CoLa_{0.1}Fe_{1.9}O_4$ nanoparticles (Figure 5(b)).

Table 6 shows that the total reduction of Congo red dye using the $CoLa_{0.1}Fe_{1.9}O_4$, i.e., 95.98% (54.61% with photocatalysis), 97.32% (60.00% with photocatalysis), and 97.90% (40.35% with photocatalysis) at the T_a of 200 °C, 300 °C, and 400 °C, respectively. Physical changes that occur in the absorption and photocatalyst process are the color change of the congo red test material from red to clear (Figure 5(c)). Furthermore, the mechanism that occurs in the dye removal process is the absorption of the material caused by the surface properties of the material. The surface properties of the material are related to the crystallite size, the smaller the crystallite size causes a large surface area, this is one of the indicators supporting the absorption process [46]. The results obtained are different due to other factors, i.e., magnetic properties such as H_C. H_C supports the absorption mechanism, the smaller the H_C, the smaller the induced magnetism that occurs in the absorption pro-

Table 6. Percentage reduction (η) of lanthanum substitution of cobalt ferrite material with variations in the T_a.

T_a (°C)	Dye Removal Properties (%)
200	95.98
300	97.32
400	97.90

cess, and the greater the absorption speed. Meanwhile, in the photocatalyst process, the mechanism that occurs follows the S-scheme, in which La^{3+} ions help in slowing down the recombination of electrons (e^-) from the conduction band (CB) to the valence band (VB) in cobalt ferrite material. Thus, the formation of reactive oxygen species (•OH, O_2^-, and H_2O_2) becomes more, especially the formation of hydroxyl ions (•OH). This formation is used to degrade pollutants in this case, namely congo red pollutant [47], the more •OH radicals formed, the better the degradation results obtained [48].

4. Conclusions

Lanthanum-substituted cobalt ferrite ($CoLa_{0.1}Fe_{1.9}O_4$) nanoparticles with the annealing temperature (T_a) treatment have been successfully synthesized using the coprecipitation method. XRD analysis shows that all the samples crystallized indicate a cubic spinel-type structure with an Fd-3m space group. FTIR analysis shows that the main absorption band range corresponds to the cobalt ferrite-based structure. VSM results show that the $CoLa_{0.1}Fe_{1.9}O_4$ nanoparticles decrease the magnitude of the H_C with increasing the T_a. This is directly correlated with the change in the anisotropy magnetic constant (K). The obtained nanoparticles also performed well for Congo red dye removal. The effect of temperature will change the physical properties which affect its application. So, as the annealing temperature increases, the crystal growth gets better.

Acknowledgments

This study was financially supported by Penelitian Hibah Grup Riset (Penelitian HGR UNS A) Universitas Sebelas Maret, Indonesia contract number: 228/UN27.22/PT.01.03/2023.

Credit Author Statement

Author Contributions: Ramadona Rahmawati: Writting Draft Preparation, Formal Analysis; Adiana Musadewi; Data Curation; Nurdiyantoro Putra Prasetya: Investigation, Resources, Data analysis, Writing, Review and Editing; Suharno: Supervision, Software; Sri Budiawanti: Data Curation; Dwi Teguh Rahardjo: Investigation; Riyatun: Review and Editing; Utari: Resources, Methodology, Review and Editing, Project Administration; Yofentina Iriani: Investigation, Resources; Nuryani: Validation; Budi Purnama: Conceptualization, Methodology, Investigation, Resources, Data Curation, Writing, Review and Editing, Supervision, Validation. All authors have read and agreed to the published version of the manuscript.

References

[1] Pubby, K., Meena, S.S., Yusuf, S.M., Bindra Narang, S. (2018). Cobalt substituted nickel ferrites via Pechini's sol–gel citrate route: X-band electromagnetic characterization. *Journal of Magnetism and Magnetic Materials*, 466, 430–445. DOI: 10.1016/j.jmmm.2018.07.038.

[2] Ghorbani, H., Eshraghi, M., Sabouri Dodaran, A.A. (2022). Structural and magnetic properties of cobalt ferrite nanoparticles doped with cadmium. *Physica B: Condensed Matter*, 634, 413816. DOI: 10.1016/j.physb.2022.413816.

[3] Zhang, W., Sun, A., Zhao, X., Pan, X., Han, Y., Suo, N., Yu, L., Zuo, Z. (2020). Structural and magnetic properties of Ni–Cu–Co ferrites prepared from sol-gel auto combustion method with different complexing agents. *Journal of Alloys and Compounds*, 816, 152501. DOI: 10.1016/j.jallcom.2019.152501.

[4] Mariosi, F.R., Venturini, J., da Cas Viegas, A., Bergmann, C.P. (2020). Lanthanum-doped spinel cobalt ferrite (CoFe2O4) nanoparticles for environmental applications. *Ceramics International*, 46(3), 2772–2779. DOI: 10.1016/j.ceramint.2019.09.266.

[5] Ai, L., Jiang, J. (2010). Influence of annealing temperature on the formation, microstructure and magnetic properties of spinel nanocrystalline cobalt ferrites. *Current Applied Physics*, 10(1), 284–288. DOI: 10.1016/j.cap.2009.06.007.

[6] Prasetya, N.P., Setiyani, R.I., Utari, Kusumandari, K., Iriani, Y., Safani, J., Taufiq, A., Wibowo, N.A., Suharno, S., Purnama, B. (2023). Cation trivalent tune of crystalline structure and magnetic properties in coprecipitated cobalt ferrite nanoparticles. *Materials Research Express*, 10(3), 036102. DOI: 10.1088/2053-1591/acc011.

[7] Al Maashani, M.S., Khalaf, K.A., Gismelseed, A.M., Al-Omari, I.A. (2020). The structural and magnetic properties of the nano-CoFe2O4 ferrite prepared by sol-gel auto-combustion technique. *Journal of Alloys and Compounds*, 817, 152786. DOI: 10.1016/j.jallcom.2019.152786.

[8] Kotnala, R.K., Shah, J. (2015). Ferrite Materials: Nano to Spintronics Regime. *Handbook of Magnetic Materials*, 23, 291–379. DOI: 10.1016/B978-0-444-63528-0.00004-8.

[9] Zheng, B., Fan, J., Chen, B., Qin, X., Wang, J., Wang, F., Deng, R., Liu, X. (2022). Rare-Earth Doping in Nanostructured Inorganic Materials. *Chemical Reviews*, 122(6), 5519–5603. DOI: 10.1021/acs.chemrev.1c00644.

[10] Jing, X., Guo, M., Li, Z., Qin, C., Chen, Z., Li, Z., Gong, H. (2023). Study on structure and magnetic properties of rare earth doped cobalt ferrite: The influence mechanism of different substitution positions. *Ceramics International*, 49(9), 14046–14056. DOI: 10.1016/j.ceramint.2022.12.286.

[11] López-Ortega, A., Lottini, E., de Julián Fernández, C., Sangregorio, C. (2015). Exploring the Magnetic Properties of Cobalt-Ferrite Nanoparticles for the Development of a Rare-Earth-Free Permanent Magnet. *Chemistry of Materials*, 27(11), 4048–4056. DOI: 10.1021/acs.chemmater.5b01034.

[12] Caltun, O.F., Rao, G.S.N., Rao, K.H., Rao, B.P., Kim, C., Kim, C.-O., Dumitru, I., Lupu, N., Chiriac, H. (2007). High Magnetostrictive Cobalt Ferrite for Sensor Applications. *Sensor Letters*, 5(1), 45–47. DOI: 10.1166/sl.2007.027.

[13] Swathi, S., Yuvakkumar, R., Kumar, P.S., Ravi, G., Velauthapillai, D. (2021). Annealing temperature effect on cobalt ferrite nanoparticles for photocatalytic degradation. *Chemosphere*, 281, 130903. DOI: 10.1016/j.chemosphere.2021.130903.

[14] Sanpo, N., Berndt, C.C., Wen, C., Wang, J. (2013). Transition metal-substituted cobalt ferrite nanoparticles for biomedical applications. *Acta Biomaterialia*, 9(3), 5830–5837. DOI: 10.1016/j.actbio.2012.10.037.

[15] Dey, C., Baishya, K., Ghosh, A., Goswami, M.M., Ghosh, A., Mandal, K. (2017). Improvement of drug delivery by hyperthermia treatment using magnetic cubic cobalt ferrite nanoparticles. *Journal of Magnetism and Magnetic Materials*, 427, 168–174. DOI: 10.1016/j.jmmm.2016.11.024.

[16] Arshad, J.M., Raza, W., Amin, N., Nadeem, K., Imran Arshad, M., Azhar Khan, M. (2021). Synthesis and characterization of cobalt ferrites as MRI contrast agent. *Materials Today: Proceedings*, 47, S50–S54. DOI: 10.1016/j.matpr.2020.04.746.

[17] Hazarika, S., Borah, G. (2022). Silica supported spinel structured cobalt ferrite multifunctional nanocatalyst for hydration of nitriles and oxidative decarboxylation of phenylacetic acids. *Applied Organometallic Chemistry*, 36(11), e6864. DOI: 10.1002/aoc.6864.

[18] Maaz, K., Mumtaz, A., Hasanain, S.K., Ceylan, A. (2007). Synthesis and magnetic properties of cobalt ferrite ($CoFe_2O_4$) nanoparticles prepared by wet chemical route. *Journal of Magnetism and Magnetic Materials*, 308(2), 289–295. DOI: 10.1016/j.jmmm.2006.06.003.

[19] Purnama, B., Rahmawati, R., Wijayanta, A.T., Suharyana (2015). Dependence of structural and magnetic properties on annealing times in co-precipitated cobalt ferrite nanoparticles. *Journal of Magnetics*, 20(3), 207–210. DOI: 10.4283/jmag.2015.20.3.207.

[20] Sajjia, M., Oubaha, M., Prescott, T., Olabi, A.G. (2010). Development of cobalt ferrite powder preparation employing the sol-gel technique and its structural characterization. *Journal of Alloys and Compounds*, 506(1), 400–406. DOI: 10.1016/j.jallcom.2010.07.015.

[21] Hashemi, S.M., Ataollahi, Z., Hasani, S., Seifoddini, A. (2023). Synthesis of the cobalt ferrite magnetic nanoparticles by sol–gel auto-combustion method in the presence of egg white (albumin). *Journal of Sol-Gel Science and Technology*, 106, 23–36. DOI: 10.1007/s10971-023-06073-2.

[22] Rahardjo, D.T., Budiawanti, S., Suharno, Iriani, Y., Supriyanto, A., Purnama, B. (2021). Temperature sintering dependence of crystalline structure in cobalt ferrite prepared by the sol-gel auto-combustion procedure. *Journal of Physics: Conference Series*, 1951(1), 012026. DOI: 10.1088/1742-6596/1951/1/012026.

[23] Priyadharsini, R., Dhamodharan, P., Venkateshwarlu, M., Manoharan, C. (2023). Influence of cobalt on magnetic, dielectric and electrochemical properties of copper ferrite nanoparticles via hydrothermal method. *Solid State Sciences*, 137, 107123. DOI: 10.1016/j.solidstatesciences.2023.107123.

[24] Moosavi, S., Zakaria, S., Chia, C.H., Gan, S., Azahari, N.A., Kaco, H. (2017). Hydrothermal synthesis, magnetic properties and characterization of $CoFe_2O_4$ nanocrystals. *Ceramics International*, 43(10), 7889–7894. DOI: 10.1016/j.ceramint.2017.03.110.

[25] Das, S., Manoharan, C., Venkateshwarlu, M., Dhamodharan, P. (2019). Structural, optical, morphological and magnetic properties of nickel doped cobalt ferrite nanoparticles synthesized by hydrothermal method. *Journal of Materials Science: Materials in Electronics*, 30(22), 19880–19893. DOI: 10.1007/s10854-019-02355-0.

[26] Jain, R., Kumar, S., Meena, S.K. (2022). Precipitating agent (NaOH and NH_4OH) dependent magnetic properties of cobalt ferrite nanoparticles. *AIP Advances*, 12(9), 095109. DOI: 10.1063/5.0098157.

[27] Zhang, Y., Yang, Z., Yin, D., Liu, Y., Fei, C., Xiong, R., Shi, J., Yan, G. (2010). Composition and magnetic properties of cobalt ferrite nano-particles prepared by the co-precipitation method. *Journal of Magnetism and Magnetic Materials*, 322(21), 3470–3475. DOI: 10.1016/j.jmmm.2010.06.047.

[28] Kamran, M., Anis-ur-Rehman, M. (2020). Enhanced transport properties in Ce doped cobalt ferrites nanoparticles for resistive RAM applications. *Journal of Alloys and Compounds*, 822, 153583. DOI: 10.1016/j.jallcom.2019.153583.

[29] Kole, A.K., Kumbhakar, P. (2012). Cubic-to-hexagonal phase transition and optical properties of chemically synthesized ZnS nanocrystals. *Results in Physics*, 2, 150–155. DOI: 10.1016/j.rinp.2012.09.010.

[30] Riyatun, R., Kusumaningsih, T., Supriyanto, A., Akmal, H.B., Zulhaina, F.M., Prasetya, N.P., Purnama, B. (2023). Nanoparticle−preparation−procedure tune of physical, antibacterial, and photocatalyst properties on silver substituted cobalt ferrite. *Results in Engineering*, 18, 101085. DOI: 10.1016/j.rineng.2023.101085.

[31] Amiri, S., Shokrollahi, H. (2013). Magnetic and structural properties of RE doped Co-ferrite (RE=Nd, Eu, and Gd) nano-particles synthesized by co-precipitation. *Journal of Magnetism and Magnetic Materials*, 345, 18–23. DOI: 10.1016/j.jmmm.2013.05.030.

[32] Pavan Kumar Chintala, J.N., Bharadwaj, S., Chaitanya Varma, M., Choudary, G.S.V.R.K. (2022). Impact of cobalt substitution on cation distribution and elastic properties of Ni–Zn ferrite investigated by X-ray diffraction, infrared spectroscopy, and Mössbauer spectral analysis. *Journal of Physics and Chemistry of Solids*, 160, 110298. DOI: 10.1016/j.jpcs.2021.110298.

[33] Purnama, B., Arilasita, R., Rikamukti, N., Utari, U., Budiawanti, S., Suharno, S., Wijayanta, A.T., Suharyana, Djuhana, D., Suharyadi, E., Tanaka, T., Matsuyama, K. (2022). Annealing temperature dependence of crystalline structure and magnetic properties in nano-powder strontium-substituted cobalt ferrite. *Nano-Structures & Nano-Objects*, 30, 100862. DOI: 10.1016/j.nanoso.2022.100862.

[34] B.D. Cullity, Graham, C.D. (2009). *Introduction to Magnetic Magnetic Materials*, Second Edition. IEEE Pres & Wiley, New Jersey, USA

[35] Abraime, B., El Maalam, K., Fkhar, L., Mahmoud, A., Boschini, F., Ait Tamerd, M., Benyoussef, A., Hamedoun, M., Hlil, E.K., Ait Ali, M., El Kenz, A., Mounkachi, O. (2020). Influence of synthesis methods with low annealing temperature on the structural and magnetic properties of $CoFe_2O_4$ nanopowders for permanent magnet application. *Journal of Magnetism and Magnetic Materials*, 500, 166416. DOI: 10.1016/j.jmmm.2020.166416.

[36] Nitika, N., Rana, A., Kumar, V., Awasthi, A.M. (2021). Effect of dopant concentration and annealing temperature on electric and magnetic properties of lanthanum substituted $CoFe_2O_4$ nanoparticles for potential use in 5G wireless communication systems. *Ceramics International*, 47(14), 20669–20677. DOI: 10.1016/j.ceramint.2021.04.077.

[37] El-Shobaky, G.A., Turky, A.M., Mostafa, N.Y., Mohamed, S.K. (2010). Effect of preparation conditions on physicochemical, surface and catalytic properties of cobalt ferrite prepared by coprecipitation. *Journal of Alloys and Compounds*, 493(1–2), 415–422. DOI: 10.1016/j.jallcom.2009.12.115.

[38] Ashour, A.H., El-Batal, A.I., Maksoud, M.I.A.A., El-Sayyad, G.S., Labib, S., Abdeltwab, E., El-Okr, M.M. (2018). Antimicrobial activity of metal-substituted cobalt ferrite nanoparticles synthesized by sol–gel technique. *Particuology*, 40, 141–151. DOI: 10.1016/J.PARTIC.2017.12.001.

[39] Kabilan, R., Ashokkumar, M. (2022). Annealing temperature enhanced visible absorption and magnetic properties of (Cu, Cr) co-doped ZnO diluted magnetic semiconductors. *Journal of Molecular Structure*, 1249, 131536. DOI: 10.1016/j.molstruc.2021.131536.

[40] Kumar, L., Kumar, P., Narayan, A., Kar, M. (2013). Rietveld analysis of XRD patterns of different sizes of nanocrystalline cobalt ferrite. *International Nano Letters*, 3(1), 1–12. DOI: 10.1186/2228-5326-3-8.

[41] Muthee, D.K., Dejene, B.F. (2021). Effect of annealing temperature on structural, optical, and photocatalytic properties of titanium dioxide nanoparticles. *Heliyon*, 7(6), e07269. DOI: 10.1016/j.heliyon.2021.e07269.

[42] Khalid Hossain, M., Pervez, M.F., Mia, M.N.H., Tayyaba, S., Jalal Uddin, M., Ahamed, R., Khan, R.A., Hoq, M., Khan, M.A., Ahmed, F. (2017). Annealing temperature effect on structural, morphological and optical parameters of mesoporous TiO2 film photoanode for dye-sensitized solar cell application. *Materials Science- Poland*, 35(4), 868–877. DOI: 10.1515/msp-2017-0082.

[43] Aslam, A., Razzaq, A., Naz, S., Amin, N., Arshad, M.I., Nabi, M.A.U., Nawaz, A., Mahmood, K., Bibi, A., Iqbal, F., Shakil, M., Farooq, Z., Iqbal, M.Z., Haider, S.S., Rehman, A. ur (2021). Impact of Lanthanum-Doping on the Physical and Electrical Properties of Cobalt Ferrites. *Journal of Superconductivity and Novel Magnetism*, 34(7), 1855–1864. DOI: 10.1007/s10948-021-05802-4.

[44] El-Ghazzawy, E.H. (2020). Effect of heat treatment on structural, magnetic, elastic and optical properties of the co-precipitated $Co_{0.4}Sr_{0.6}Fe_2O_4$. *Journal of Magnetism and Magnetic Materials*, 497, 166017. DOI: 10.1016/j.jmmm.2019.166017.

[45] Chandra Sekhar, D., Subba Rao, T., Chandra Babu Naidu, K. (2020). Iron deficient $BaNi_xMn_xFe_{12-2x}O_{19}$ (x = 0.0–0.5) hexagonal plates: single-domain magnetic structure and dielectric properties. *Applied Physics A: Materials Science and Processing*, 126(7), 1–8. DOI: 10.1007/s00339-020-03681-5.

[46] Ibrahim, S.M., Badawy, A.A., Essawy, H.A. (2019). Improvement of dyes removal from aqueous solution by Nanosized cobalt ferrite treated with humic acid during coprecipitation. *Journal of Nanostructure in Chemistry*, 9(4), 281–298. DOI: 10.1007/s40097-019-00318-9.

[47] Bao, Y., Song, S., Yao, G., Jiang, S. (2021). S-Scheme Photocatalytic Systems. *Solar RRL*, 5(7), 1–13. DOI: 10.1002/solr.202100118.

[48] Dong, S., Feng, J., Fan, M., Pi, Y., Hu, L., Han, X., Liu, M., Sun, J., Sun, J. (2015). Recent developments in heterogeneous photocatalytic water treatment using visible light-responsive photocatalysts: A review. *RSC Advances*, 5(19), 14610–14630. DOI: 10.1039/c4ra13734e.